



# Tuning $\text{Ti}^{\delta+}$ - $\text{Vo}^{2+}$ - $\text{Pt}^{\delta+}$ interfaces over $\text{Pt}/\text{TiO}_2$ catalysts for efficient photocatalytic oxidation of toluene

Lijun Yan, Qing Wang, Wenqiang Qu, Tingting Yan, Hongrui Li, Penglu Wang\*,  
Dengsong Zhang\*

School of Environmental and Chemical Engineering, International Joint Laboratory of Catalytic Chemistry, College of Sciences, Shanghai University, Shanghai 200444, PR China



## ARTICLE INFO

**Keywords:**  
Toluene degradation  
Volatile organic compounds  
Photocatalysis  
Air purification

## ABSTRACT

Promoting the ring-opening process is vital to increase the mineralization of aromatic volatile organic compounds. Rational regulation of metal-support interaction is essential for the opening of the aromatic ring over  $\text{Pt}/\text{TiO}_2$  catalysts. Herein, the  $\text{Pt}/\text{TiO}_2$ -C catalyst with  $\text{Ti}^{\delta+}$ - $\text{Vo}^{2+}$ - $\text{Pt}^{\delta+}$  interface obtained by reverse electron transfer is successfully regulated via reduction-oxidation treatment for efficient photocatalytic degradation of toluene. This structure accelerates the pre-activation of toluene to generate abundant reactive intermediate species for the photocatalysis reaction. On the other hand, the special interface endows  $\text{Pt}/\text{TiO}_2$ -C the ability to produce more reactive oxygen species under illumination, which can synergistically promote the direct opening of benzene ring. The  $\text{Pt}/\text{TiO}_2$ -C shows a stronger oxidation capacity and a mineralization rate 15% higher than the traditional  $\text{Pt}/\text{TiO}_2$ . This work proves that reduction-oxidation treatment is an effective approach to modify catalysts for air purification and provides a novel idea for the degradation of other aromatic volatile organic pollutants.

## 1. Introduction

Air pollution has received considerable attention in contemporary society [1]. Volatile organic compounds (VOCs), as typical pollutants, seriously threaten air quality and human health [2–4]. Photocatalytic oxidation is an effective strategy for air purification based on the strong oxidation capacity at mild conditions, especially for the degradation of low concentration VOCs (benzene series [5–7], alcohol [8] and aldehydes [9]). Among these pollutants, toluene is relatively difficult to be degraded due to the high stability of the benzene ring conjugated  $\pi$  system [10]. Therefore, it remains a challenge for photocatalytic degradation of toluene to realize the ring-opening reaction.

$\text{TiO}_2$  photocatalyst has been widely adopted in environmental remediation because of its cheapness and good oxidative capacity. However, the redox reaction influenced by the high photogenerated carrier recombination rate has the low mineralization efficiency of VOCs. The existence of noble metals (such as Pt) can inhibit the recombination of charge carriers, which will effectively improve the performance of catalysts [11,12]. Generally, the metal-support interaction (MSI) is a common phenomenon for supported metal catalysts, which can effectively modify the electronic properties of metal

nano-particles (NPs) and supports, thus expressing an important influence on the performance of catalysts [13–15]. Basically, MSI can be regulated by modifying the composition and the morphology of the support, controlling the size and component of the metal particles, or using different treatment methods (such as being reduced at different temperatures, reduction-oxidation cycle and overlayer deposition) to treat the catalysts. For example, Zhu et al. design the defect sites of h-BN to regulate the MSI between Pt and BN, finding that Pt combined with N vacancy has higher CO oxidation activity than that bonding with B vacancy [16]. MSI is also closely related to the size of metal particles. Guo et al. observe that as the size of Ru particles decreases from 4 nm to 1 nm, the electronic MSI between Ru and  $\text{CeO}_2$  gradually increases, which improves the  $\text{CO}_2$  activation ability of catalysts [17]. On the other hand, the reduction-oxidation-reduction methods are adopted to control the MSI between Co and reducible support ( $\text{TiO}_2$ ,  $\text{Nb}_2\text{O}_5$ ), it is found that this treatment could expose more active Co particles while inheriting the enhancing effect of the reduced oxide [18]. However, too strong metal-support interaction will enhance the reduction capability of the catalysts, which is detrimental to the oxidation of toluene [19]. To solve this problem, it is promising to increase oxidation capacity by regulating the MSI, but the specific method is still unclear.

\* Corresponding authors.

E-mail addresses: [plwang@shu.edu.cn](mailto:plwang@shu.edu.cn) (P. Wang), [dszhang@shu.edu.cn](mailto:dszhang@shu.edu.cn) (D. Zhang).

Recently, notable progress has been made in the research on the method of regulating the MSI, aiming at the promoted performance of supported metal catalysts. It is reported that the oxidation treatment can reverse the strong metal-support interaction, which will lead to the reversible structural changes of the catalysts [20]. Matsui et al. find that the successive reduction–oxidation treatment can weaken the strong metal-support interaction, and contribute to the rearrangement of atoms on the catalyst surface, thereby improving the catalytic performance of methane combustion and CO oxidation [21]. Similarly, Gänzler et al. utilize the reduction–oxidation treatment to control the particle size and oxidation state of metal NPs and further improve the CO catalytic oxidation activity [22]. It can be seen that reduction–oxidation treatment is beneficial for promoting the oxidation process by adjusting MSI. In general, increasing the oxidation capacity can accelerate the benzene ring opening on the catalyst [23]. Therefore, reduction–oxidation treatment is expected as an effective method to enhance the ability to photocatalytic degradation of toluene.

In this paper, we take a novel approach to controllably regulate the Ti-O-Pt interface of Pt/TiO<sub>2</sub> using reduction–oxidation treatment to promote the photocatalytic oxidation of toluene. The electrons between Pt and TiO<sub>2</sub> are transferring in the opposite direction after the reduction–oxidation treatment, which can result in the generation of single-electron-trapped oxygen vacancies (SETOVs, labeled as Vo<sup>·</sup>). The combination study of X-ray photoelectron spectroscopy, Diffuse Reflectance Infrared Fourier Transform spectroscopy of chemisorbed CO, electron paramagnetic resonance, *in situ* Raman, and *in situ* Diffuse Reflectance Infrared Fourier Transform Spectroscopy confirms that a specific Ti<sup>δ+</sup>-Vo<sup>·</sup>-Pt<sup>δ+</sup> interface is formed and it is beneficial to promote fast activation of toluene chemisorbed on the catalyst surface. In addition, more reactive oxygen species (ROS) with strong oxidation capacity are generated and can directly attack the aromatic ring in the process of toluene mineralization. Our work elucidates the ring-opening mechanism of toluene degradation and provides a new train of thought in photocatalytic toluene conversion.

## 2. Experimental section

### 2.1. Catalysts preparation

Pt/TiO<sub>2</sub> photocatalysts are prepared by different processing methods. Briefly, 3.0 g of TiO<sub>2</sub> (99.8%, Shanghai Aladdin Biochemical Technology Co., Ltd., CAS: 13463-67-7), 0.996 mL of H<sub>2</sub>PtCl<sub>6</sub>·6H<sub>2</sub>O solution (1.506 mg/mL), and 30 mL of deionized water are mixed in a glass container and stirred at 323 K for 40 min. Then the excess water is rotary evaporated, and the sample is dried at 353 K for 8 h. Then the residue is separated and treated by reduction (10% H<sub>2</sub>/N<sub>2</sub> for 2 h at 673 K) or reduction accompanied by successive calcination (673 K for 2 h, air) process. The sample reduced alone is named Pt/TiO<sub>2</sub>, and the sample exposed by reduction and successive calcination treatments is nominated as Pt/TiO<sub>2</sub>-C.

### 2.2. Characterization

X-ray diffraction (XRD) is tested on a Bruker D8 Advance diffractometer with a Cu K $\alpha$  radiation and a LynxEye-XE-T linear detector. The scanning speed is 10°·min<sup>-1</sup>. The morphology is observed by high-resolution transmission electron microscopy (HRTEM, JEM-2100F, JEOL LTD, Japan). The specific surface area is measured on a nitrogen adsorption instrument (Micromeritics ASAP 2460, America). The surface electronic states and valence band position are measured by X-ray photoelectron spectroscopy (XPS) and Valance band-XPS (Vb-XPS, Kratos Axis DLD, Japan) respectively. Raman and *in situ* Raman spectra are taken in a Horiba Raman spectrometer (LabRAM HR Evolution, France) with 633 nm laser as the excitation source. A UV-vis spectrophotometer with diffuse reflectance accessory (UV-vis DRS, Cary5000, Agilent, USA) is used to record the UV-vis spectral data (using BaSO<sub>4</sub> as

a reference). Electron paramagnetic resonance (EPR, EMX-8/2.7, Bruker, American) is carried out to verify the existence of lone pair electrons. The radical capture test is performed at room temperature and 5,5-dimethyl-1-pyrrolidine N-oxide (DMPO) is used as a free radical scavenger. The •OH and •O<sub>2</sub><sup>·</sup> signals are captured in an aqueous solution and methanol, respectively. The adducts of DMPO-•OH and DMPO-•O<sub>2</sub><sup>·</sup> produced by UV irradiation are recorded every five minutes. The surface photovoltage (SPV) is measured in a self-installed instrument consisting of light source (CHF-XM500, Changtu Technology Co., Ltd.), monochromator (SBP300, Zolix Instrument Co., Ltd.) and lockin amplifier (SR830, Stanford research systems, Inc.). The diffuse reflectance infrared Fourier transform spectroscopy of chemisorbed CO (CO-DRIFTS) experiments are carried out on a Bruker VERTEX 80v Fourier transformed infrared spectrometer to explore the structure of the catalysts. *In situ* diffuse reflectance infrared Fourier transform spectroscopy (*in situ* DRIFTS) is obtained on a Fourier-transform infrared spectrometer (Thermo Fisher, USA, Nicolet is50) with a MCT/A detector. Photoluminescence (PL) spectra are gathered to characterize the fluorescence intensity of samples using a fluorescence spectrometer with an excitation wavelength of 320 nm (FS-5, Edinburgh).

### 2.3. Photocatalytic activity tests

For the real-time supervision of the photocatalytic performance of the catalysts, 0.2 g sample is evenly dispersed on four pieces of quartz plates in the continuous stream reactor with deionized water as a wetting agent and then dried in 353 K oven. The dried quartz plates are put into a reactor equipped with a 300 W ultraviolet lamp. In the process of toluene adsorption, the flow rate of dry air (150 mL/min) and wet air (134 mL/min) is controlled by the mass flowmeter and then mixed to obtain the diluted toluene. After reaching the adsorption equilibrium, the light irradiation is introduced and continued for 30 min. The concentration of toluene and CO<sub>2</sub> is monitored by a photoacoustic spectrometer analyzer (GASERA ONE, Beijing Duke Technology Co., Ltd.) (**Scheme S1**).

### 2.4. *In situ* Raman

*In situ* Raman spectra are obtained on the LabRAM HR Evolution. The spectra in the range of 100–800 cm<sup>-1</sup> are collected to study the structure changes during toluene adsorption and photolysis reaction, and a laser with a wavelength of 633 nm is employed. The fresh catalysts are firstly pretreated under N<sub>2</sub> (30 mL/min) at 373 K for 20 min, then toluene (10 mL/min) is introduced and pre-adsorbed on the catalysts for 20 min. After that, the UV light (300 W UV lamp) is illuminated for 30 min. The Raman spectra are collected every 10 min with the resolution of 4 cm<sup>-1</sup>.

### 2.5. *In situ* DRIFTS

*In situ* DRIFTS are tested on a Nicolet is50 FT-IR spectrometer. First, the fresh catalysts are pretreated under N<sub>2</sub> (30 mL/min) at 373 K for 20 min, then the background spectra are collected at room temperature after cooling down. After that, toluene (10 mL/min) is adsorbed on the catalysts for 30 min, and the data point is collected every 2 min. Finally, the catalysts are continuously illuminated for 30 min (300 W UV lamp), and the corresponding spectra are obtained every fixed time. To observe the intermediate species, the spectra are recorded every 15 min and analyzed using a calibrated chromatography-mass spectrometry (GC-MS) system (Agilent Technology, USA, 7890B GC System and 5977).

## 3. Results and discussion

### 3.1. Morphology and structure of the catalysts

To examine the crystal phases and structures, the prepared Pt/TiO<sub>2</sub>-C

and Pt/TiO<sub>2</sub> are analyzed by XRD (Fig. S1). All diffraction peaks from the catalysts match well with the anatase and rutile TiO<sub>2</sub> phase (PDF No. 99-0008). The peaks of Pt species are not detected, ascribable to the low Pt loading (0.02 wt%) on the titanium dioxide support (Fig. S2). HRTEM is further used to study the morphology of Pt NPs in the prepared samples (Fig. S3). The lattice plane spacing of 0.22 nm in a single Pt particle can be observed, attributed to the (111) plane of Pt [24]. Additionally, a lattice fringe with 0.35 nm corresponding to the (101) plane of TiO<sub>2</sub> is also observed [25]. As for Pt/TiO<sub>2</sub>, the Pt NPs are found to be partially covered by TiO<sub>2</sub>, which indicates that the occurrence of strong metal-support interaction between TiO<sub>2</sub> and Pt in the reductive atmosphere [26]. After Pt/TiO<sub>2</sub> undergoes calcination in air, the TiO<sub>2</sub> overlayer disappears, which indicates that the interfacial interaction of the Pt/TiO<sub>2</sub>-C has changed and has also been proved by similar research over Au/TiO<sub>2</sub> system previously [27,28].

The surface electronic structures of Pt/TiO<sub>2</sub>-C and Pt/TiO<sub>2</sub> are further examined by XPS. The XPS spectra of Ti 2p (Fig. 1a) are composed of two individual peaks at 458.9 eV and 464.6 eV, which derive from Ti<sup>4+</sup> 2p<sub>3/2</sub> and Ti<sup>4+</sup> 2p<sub>1/2</sub> respectively, coinciding well with the typical characteristics of Ti-O-Ti bonds in TiO<sub>2</sub> [29]. Compared with TiO<sub>2</sub> (Fig. S4), the Ti 2p<sub>1/2</sub> peaks of Pt/TiO<sub>2</sub>-C and Pt/TiO<sub>2</sub> have a negative shift of 0.3 eV and 0.5 eV, respectively. The peak shift (0.5 eV) of Pt/TiO<sub>2</sub> is related to the reduced Ti<sup>3+</sup> around oxygen vacancies (Vo) [30], so it can be inferred that the shift (0.3 eV) of Pt/TiO<sub>2</sub>-C corresponds to a valence state between Ti<sup>3+</sup> and Ti<sup>4+</sup> (Ti<sup>δ+</sup>, 3 < δ < 4). Moreover, the asymmetric O 1s spectra exhibit three peaks at binding energy (BE) of around 530, 531, and 533 eV in TiO<sub>2</sub>, which are ascribed to lattice oxygen (O<sub>B</sub>, i.e., Ti-O-Ti), surface adsorbed oxygen (O<sub>A</sub>, i.e., O<sup>-</sup>, O<sub>2</sub><sup>-</sup>, or O<sub>2</sub><sup>2-</sup>), and surface hydroxyl species (Fig. S5), respectively [31,32]. Similar to the Ti 2p spectra, the O 1s BE of Pt/TiO<sub>2</sub>-C and Pt/TiO<sub>2</sub> also shift to the lower direction than that of TiO<sub>2</sub>, further proving the electron transfer in the Pt-TiO<sub>2</sub> binary system. As shown in Fig. 1b, the Pt 4f<sub>7/2</sub> spectra of Pt/TiO<sub>2</sub> are split into two peaks with the BE located at 70.1 eV and 72.6 eV, suggesting the existence of Pt<sup>0</sup> and Pt<sup>2+</sup> [33,34]. The proportions of Pt<sup>0</sup> and Pt<sup>2+</sup> are about 23% and 77%, respectively (Table S1). The peaks at 72.6 eV and 73.7 eV correspond to Pt<sup>2+</sup> 4f<sub>7/2</sub> and Pt<sup>δ+</sup> 4f<sub>7/2</sub> (2 < δ < 4) in Pt/TiO<sub>2</sub>-C [34,35], in which the ratio of Pt<sup>2+</sup> and Pt<sup>δ+</sup> are about 34% and 66% respectively. These phenomena suggest that the MSI between TiO<sub>2</sub> and Pt in Pt/TiO<sub>2</sub>-C is successfully regulated while special species like Ti<sup>δ+</sup> and Pt<sup>δ+</sup> are produced.

To further explore the electronic environment of adjacent Pt atoms, CO-DRIFTS is acquired as shown in Fig. 2. The CO-DRIFTS of all samples

can be classified into two major parts. As shown in Fig. 2a, the first type of peaks at 2117 and 2171 cm<sup>-1</sup> are correlated to the adsorption of gaseous CO [36]. In addition to gaseous CO, relatively weak adsorption at 1900–2010 cm<sup>-1</sup> are ascribed to linearly bound CO on Pt [37]. The linear adsorption peaks are deconvoluted into three peaks corresponding to CO adsorbed on different unsaturated Pt atom sites (i.e., terrace sites, step sites, and corner sites) [38]. Compared with Pt/TiO<sub>2</sub>, a blueshift of CO band is found in CO-DRIFTS over Pt/TiO<sub>2</sub>-C in Fig. 2b, indicating the weaker strength of Pt-CO bond owing to the lower extent of reverse donation from Pt. It means the electron density of Pt in Pt/TiO<sub>2</sub>-C is lower than that of Pt/TiO<sub>2</sub> [39]. Combined with the results of XPS above, for Pt/TiO<sub>2</sub>, strong metal-support interaction will cause electron transfer from support to metal, which increases the electron density of Pt [26]. The decrease in the electron density of Pt on Pt/TiO<sub>2</sub>-C is due to the electron transfer from Pt to TiO<sub>2</sub>, that is, a reverse electron transfer occurs between the metal and support. Interestingly, the occurrence of reverse electron transfer cannot prompt Ti to be in an electron-rich state based on the results of Ti XPS, which may result from a change in the coordination environment inside TiO<sub>2</sub>.

In Fig. 3a, UV-vis DRS of TiO<sub>2</sub> exhibits the absorption edge in the ultraviolet region ( $\lambda < 400$  nm), while a new broad peak is observed clearly at 480 nm for Pt/TiO<sub>2</sub>, suggesting the existence of Ti<sup>3+</sup> which can increase the optical absorption of the catalysts [40]. However, the absorption edge of Pt/TiO<sub>2</sub>-C has a blueshift compared with Pt/TiO<sub>2</sub>, which further verifies the formation of Ti<sup>δ+</sup>. Raman spectroscopy is further used to study the structure of Pt/TiO<sub>2</sub>-C and Pt/TiO<sub>2</sub>. Fig. 3b shows the four typical peaks between 100 and 800 cm<sup>-1</sup> (intense bands at around 142, 393, 513, and 638 cm<sup>-1</sup>, respectively), which can be assigned to the stretching modes of Ti-O band in anatase phase TiO<sub>2</sub> [41]. On the other hand, the principal peak of Pt/TiO<sub>2</sub>-C (141 cm<sup>-1</sup>) is red-shifted compared with Pt/TiO<sub>2</sub> (143 cm<sup>-1</sup>), which suggests the strength of Ti-O bond decreases. The bond strength of different samples is calculated by Hooke's law (Table S2). This longer Ti-O bond length, in turn, leads to a low electron density in its proximity, which may promote the electron transfer from Ti to Vo, then leading to the generation of Vo with localized electrons in Pt/TiO<sub>2</sub>-C [42].

EPR is further performed to study the unpaired electron spins of Vo (Fig. 3c). The Pt/TiO<sub>2</sub> exhibits the g value signal of 1.999, attributed to the paramagnetic Ti<sup>3+</sup> centers [43]. The presence of Ti<sup>3+</sup> is generally related to the generation of Vo in the reduction progress. Beyond that, Pt/TiO<sub>2</sub> displays another two EPR signals with the g value at 2.02 and 2.04. The former g value of 2.02 is ascribed to the surface O<sub>2</sub><sup>-</sup> species produced by O<sub>2</sub> adsorbing on surface Ti<sup>3+</sup> [44], while the signal at g =

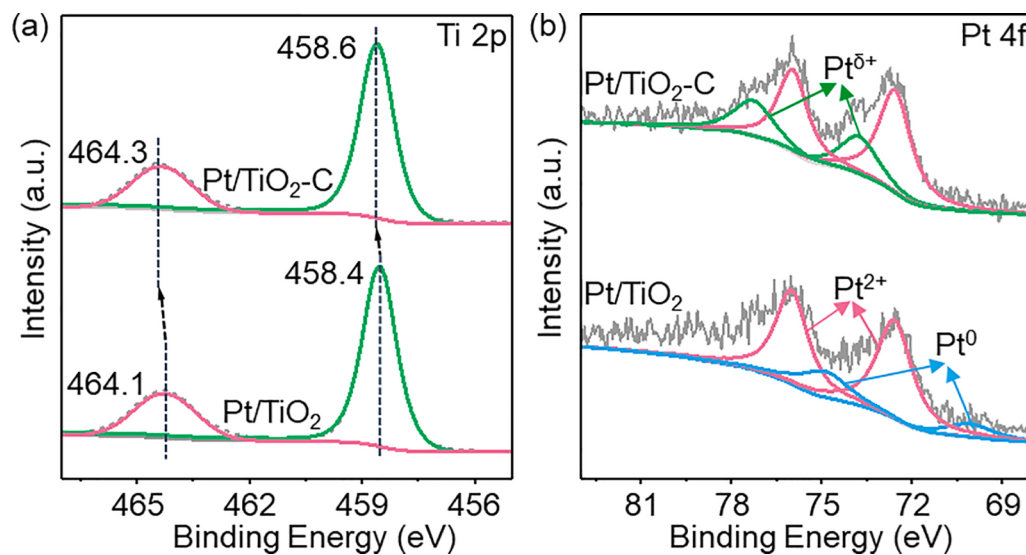


Fig. 1. XPS spectra of (a) Ti 2p and (b) Pt 4f for Pt/TiO<sub>2</sub> and Pt/TiO<sub>2</sub>-C.

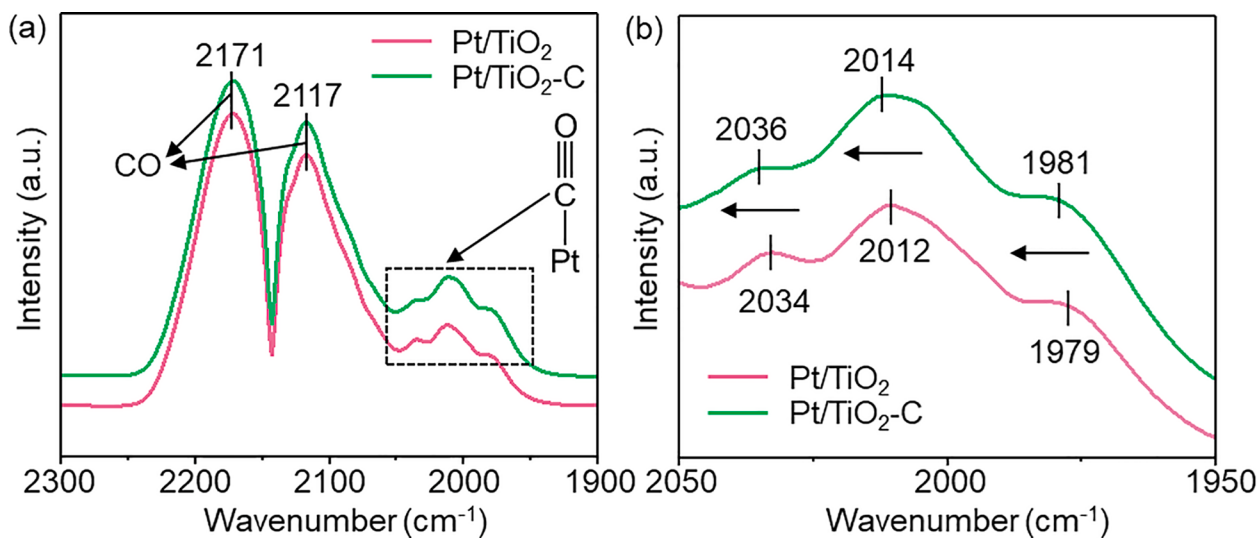


Fig. 2. (a) CO-DRIFTS and (b) partial enlargement of CO-DRIFTS from 1950 to 2050 cm<sup>-1</sup> over Pt/TiO<sub>2</sub> and Pt/TiO<sub>2</sub>-C.

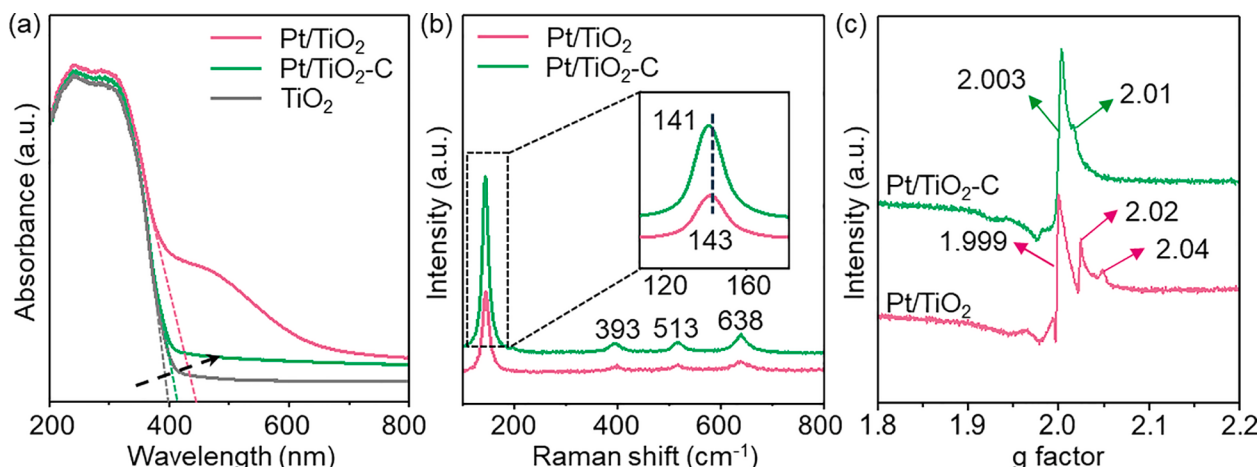


Fig. 3. (a) UV-vis DRS of different samples; (b) Raman spectra (insert: the magnified image of the main spectra in the area of 110–180 cm<sup>-1</sup>) and (c) EPR spectra of Pt/TiO<sub>2</sub> and Pt/TiO<sub>2</sub>-C.

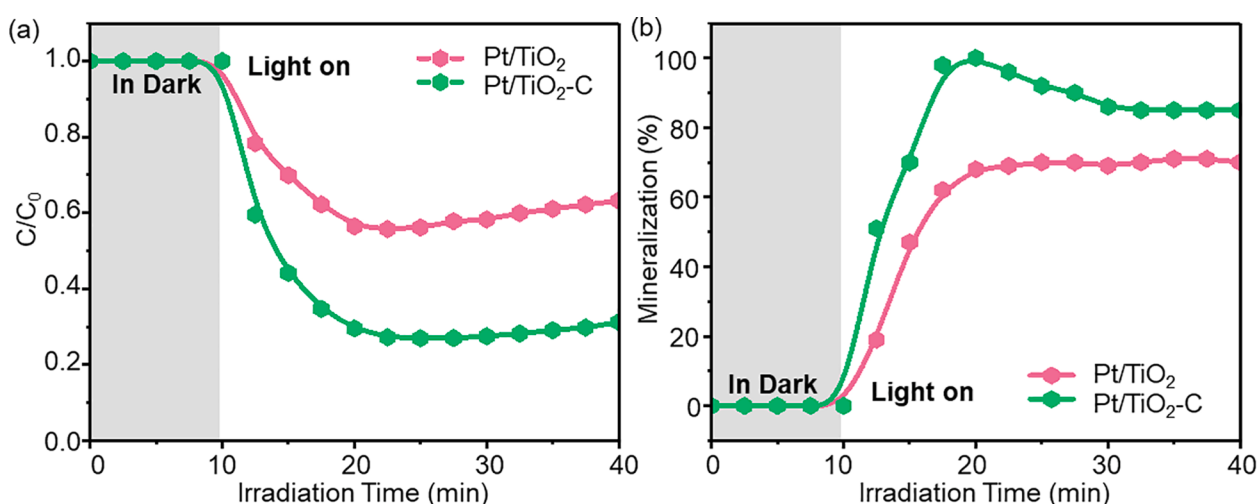


Fig. 4. (a) Photocatalytic degradation rate and (b) mineralization rate of Pt/TiO<sub>2</sub>, Pt/TiO<sub>2</sub>-C towards gas toluene under the irradiation with 300 W UV light. Reaction conditions: 1000 ppm toluene + air balanced, total flow rate 300 mL/min, and GHSV = 90000 mL/(g<sub>cat</sub>·h).

2.04 suggests the presence of  $\text{O}^-$  formed by the adsorbing of  $\text{O}_2$  on surface  $\text{Vo}$  [44]. Notably, an EPR signal at  $g = 2.003$  can be detected in  $\text{Pt}/\text{TiO}_2\text{-C}$ , which is assigned to  $\text{Vo}$ . [45]. It should be noted that the  $\text{Vo}$ -formation is accompanied by the formation of  $\text{Ti}^{\delta+}$ , and this back-donation of electrons is favorable for the oxidation reaction of the reactants [46]. Besides, the signal noted at  $g = 2.01$  is assigned to the trapped electrons on  $\text{Vo}$  [47]. This may be affected by the anisotropy of the hyperfine coupling interaction of unpaired electrons around the  $\text{Vo}$ . Nevertheless, the signals at  $g = 2.02$  and  $g = 2.04$  disappear after calcination of  $\text{Pt}/\text{TiO}_2$ . Combined with the XPS spectra, this indicates the changes of chemical state of initial  $\text{Vo}$  and the possible electron transfer from  $\text{Ti}$  to  $\text{Vo}$ . These results prove that the  $\text{Ti}^{\delta+}\text{-}\text{Vo}\text{-}\text{Pt}^{\delta+}$  interface is formed based on the reverse electron transfer in  $\text{Pt}/\text{TiO}_2\text{-C}$ , in which  $\text{Pt}^{\delta+}$  and  $\text{Vo}^-$  can synergistically promote the catalytic oxidation of toluene.

### 3.2. Photocatalytic performance of the catalysts

The photocatalytic performance of these catalysts for the removal of toluene under UV light is tested in the continuous flow reactor. It is obvious that  $\text{Pt}/\text{TiO}_2\text{-C}$  possesses a faster degradation rate of toluene than  $\text{Pt}/\text{TiO}_2$  (Fig. 4a and 4b), which indicates that  $\text{Pt}/\text{TiO}_2\text{-C}$  has better catalytic activity. The performance test results of the catalyst at different space velocities show that the degradation rate of the  $\text{Pt}/\text{TiO}_2\text{-C}$  can reach 96% under certain conditions (Fig. S6). On the other hand, the mineralization rate of  $\text{Pt}/\text{TiO}_2\text{-C}$  is as high as 85%, which is better than  $\text{Pt}/\text{TiO}_2$  (70%) and  $\text{TiO}_2$  (43%, Fig. S7). Owing to the degradation of the toluene adsorbed on the catalyst surface, the mineralization rate of the

catalysts will be higher than the degradation rate. The long-time stability of the catalysts is also tested (Fig. S8). The reason for the activity decrease of the catalysts is that a certain amount of intermediate species accumulate under UV light irradiation, thereby slightly blocking the active sites on the catalyst surface. However, the mineralization rate remains relatively stable, which may be the result of the existence of the special  $\text{Ti}^{\delta+}\text{-}\text{Vo}\text{-}\text{Pt}^{\delta+}$  interface. To further explore the stability of  $\text{Ti}^{\delta+}\text{-}\text{Vo}\text{-}\text{Pt}^{\delta+}$ , the Raman and XPS spectra of the  $\text{Pt}/\text{TiO}_2\text{-C}$  after the 60 min reaction is detected (Fig. S9 and S10). The Raman results show that there is no significant change in the catalyst structure before and after the reaction. The XPS data reveal that although the BE of  $\text{Pt}$  and  $\text{Ti}$  species shift slightly, they are still in the corresponding intermediate valence state, proving that the special interface of  $\text{Ti}^{\delta+}\text{-}\text{Vo}\text{-}\text{Pt}^{\delta+}$  is maintained. The above results indicate that  $\text{Pt}/\text{TiO}_2\text{-C}$  has significant advantages in the degradation and mineralization of toluene, and further suggest that the formation of  $\text{Ti}^{\delta+}\text{-}\text{Vo}\text{-}\text{Pt}^{\delta+}$  interface structure can effectively promote the toluene decomposition.

UV-vis DRS is further used to study the optical properties of the catalysts (Fig. 5a), the inset represents the Kubelka-Munk transformed reflectance spectra for bandgap energies. Among them, the bandgaps of  $\text{Pt}/\text{TiO}_2\text{-C}$  and  $\text{Pt}/\text{TiO}_2$  are 3.16 eV and 3.09 eV, respectively. It is known that the oxidation capability of photocatalysts depends on the energy position of the valence band (VB) to a certain extent. The relative position of VB is further verified by Vb-XPS. It can be observed that the VB potential of  $\text{Pt}/\text{TiO}_2\text{-C}$  shifts towards a more positive direction (2.23 eV) compared with  $\text{Pt}/\text{TiO}_2$  (1.93 eV) in Fig. 5b, indicating that  $\text{Pt}/\text{TiO}_2\text{-C}$  has a stronger oxidation capacity. The separation of photogenerated charge between the interface of catalysts is further explored by surface

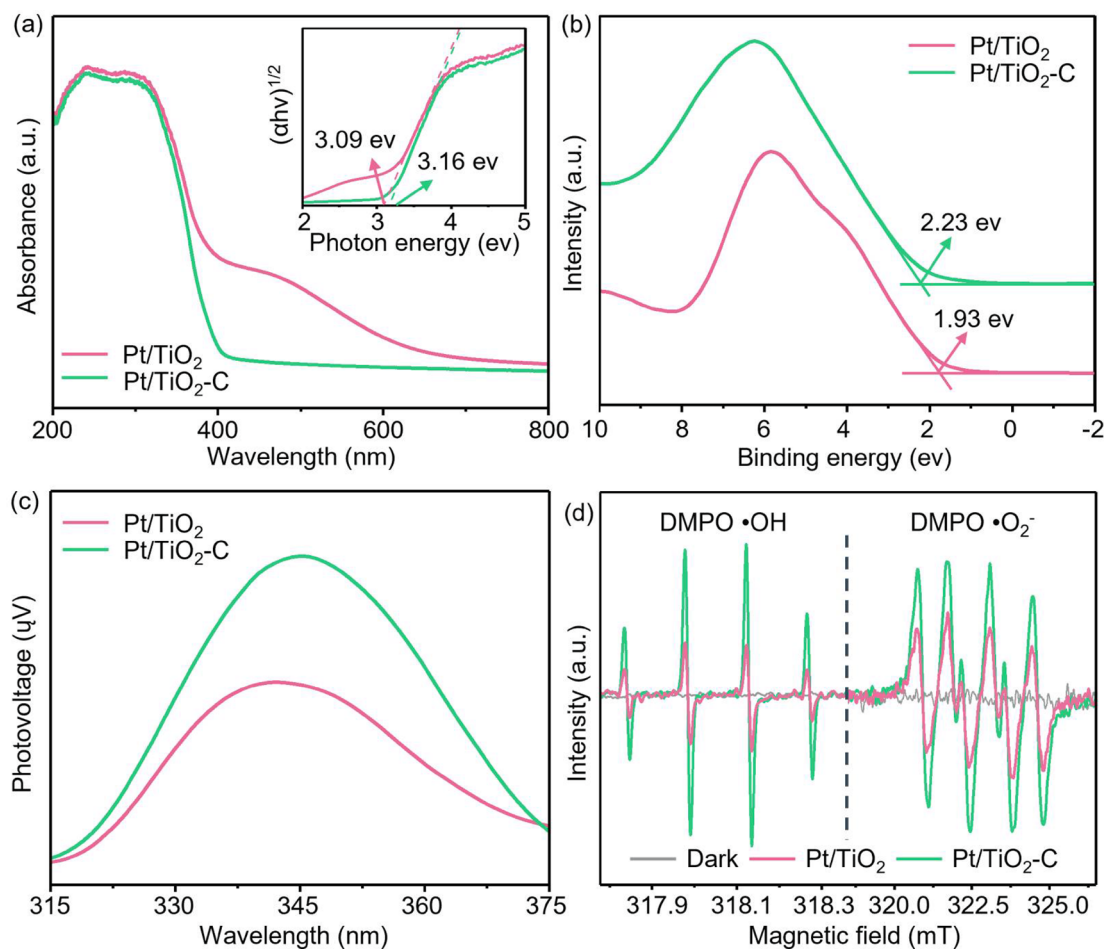


**Fig. 5.** (a) UV-vis DRS (insert: the corresponding Kubelka-Munk transformed reflectance spectra for bandgap energies); (b) Vb XPS spectra; (c) SPV spectra and (d) EPR spectra of DMPO-•OH and DMPO-•O<sub>2</sub><sup>-</sup> under UV irradiation of  $\text{Pt}/\text{TiO}_2$  and  $\text{Pt}/\text{TiO}_2\text{-C}$ .

photovoltage (SPV) technology. The Pt/TiO<sub>2</sub>-C exhibits a stronger SPV response under UV irradiation of 300–370 nm (Fig. 5c), indicating that the photogenerated charges are effectively separated. Therefore, the regulation of the Ti<sup>δ+</sup>-Vo-Pt<sup>δ+</sup> interface structure promotes the downward shift of the energy band over the Pt/TiO<sub>2</sub>-C, which further facilitates the separation of surface charge carriers and the generation of ROS. The EPR spin-trapping technique with DMPO (•OH, •O<sub>2</sub><sup>−</sup>) is then utilized to identify ROS in the process of photocatalysis (Fig. 5d). The signal cannot be detected in the dark. The characteristic peaks of DMPO-•OH and DMPO-•O<sub>2</sub><sup>−</sup> adducts are observed under UV light irradiation. This is due to the reduction and oxidation of O<sub>2</sub> and H<sub>2</sub>O adsorbed on the catalyst surface. O<sub>2</sub> are reduced by photoelectrons to generate superoxide radicals (•O<sub>2</sub><sup>−</sup>), and hydroxyl radicals (•OH) are formed via the H<sub>2</sub>O oxidation by photogenerated holes. Compared with Pt/TiO<sub>2</sub>, Pt/TiO<sub>2</sub>-C has much stronger signal of •OH and •O<sub>2</sub><sup>−</sup>. •OH are considered to be the most effective ROS in the photooxidation reaction, so Pt/TiO<sub>2</sub>-C with more •OH are conducive to the degradation of toluene. Furthermore, the more •O<sub>2</sub><sup>−</sup> may be formed by the conversion of •OH on the VB via the path of •OH → H<sub>2</sub>O<sub>2</sub> → •O<sub>2</sub><sup>−</sup> [48]. This implies that the excellent catalytic performance of toluene is mainly related to the existence of the unique Ti<sup>δ+</sup>-Vo-Pt<sup>δ+</sup> interface structure, which regulates the stronger oxidation capability of the Pt/TiO<sub>2</sub>-C and induces more ROS to participate in the degradation of toluene.

### 3.3. Mechanism for photocatalytic degradation of toluene over the catalysts

The specific surface area of Pt/TiO<sub>2</sub>-C is similar with Pt/TiO<sub>2</sub> (Fig. S11), for another, temperature programmed desorption of Toluene with mass spectrum (Toluene-TPD-MS) reveals that the weaker toluene adsorption of Pt/TiO<sub>2</sub>-C, which is related to the secondary calcination progress (Fig. S12, S13 and Table S3). Moreover, the specific toluene adsorption behaviors are investigated via *in situ* DRIFTS. Species like -OH (3702, 3370 cm<sup>−1</sup>) [49], -C = O (1577, 1658 cm<sup>−1</sup>) [50], -CHO (1540 cm<sup>−1</sup>) [51], and aromatic ring (1460 cm<sup>−1</sup>) [52] are detected during the adsorption process of toluene (Fig. S14), which is attributed to the pre-activation of toluene. Furthermore, as shown in Fig. 6, peak intensity around 1540 and 1577 cm<sup>−1</sup> for Pt/TiO<sub>2</sub>-C is stronger than Pt/TiO<sub>2</sub>, suggesting that the more accumulation of pre-activated products (i.e., benzaldehyde and benzoic acid intermediate species) on the catalyst surface. From the correlation curve between the peak intensity of the intermediate species and time (Fig. S15), it can be clearly seen that

the production rate of reactive intermediates on Pt/TiO<sub>2</sub>-C is faster than that of Pt/TiO<sub>2</sub>. To investigate the relationship between toluene adsorption and activation, *in situ* Raman spectra of the catalysts are collected (Fig. 7). Compared with TiO<sub>2</sub> (Fig. S16), the changes in the Raman spectra of Pt/TiO<sub>2</sub>-C and Pt/TiO<sub>2</sub> are associated with the existence of structural disorder in TiO<sub>2</sub> crystal [53], which corresponds to the local structure of Ti<sup>δ+</sup>-Vo and Ti<sup>3+</sup>-Vo, respectively. In Pt/TiO<sub>2</sub>-C (Fig. 7b), the blueshift of the peaks at 141 cm<sup>−1</sup> to 144 cm<sup>−1</sup> is due to the increase of electron density around Ti<sup>δ+</sup>-Vo, which is related to the electrons donation from -CH<sub>3</sub> to Ti<sup>δ+</sup>-Vo for pre-activation of toluene [42]. After -CH<sub>3</sub> gives an electron, toluene tends to lose a proton to form a benzyl radical, which is an important intermediate for subsequent reaction and will facilitate the conversion of toluene [54]. On the contrary, the decline of electron density inferred from the redshift from 143 cm<sup>−1</sup> to 141 cm<sup>−1</sup> is detrimental to the activation of toluene in Pt/TiO<sub>2</sub> (Fig. 7a). Moreover, from the UV-vis spectra of toluene adsorption (Fig. S17), a redshift (229 → 233 nm) is observed on Pt/TiO<sub>2</sub>-C compared with Pt/TiO<sub>2</sub> when toluene is introduced, which suggests the stronger charge-transfer transition from O 2p to Ti 3d [55]. Combined with the above results, it can be concluded that the faster pre-activation reaction has occurred on Pt/TiO<sub>2</sub>-C. This provides abundant intermediate species for the subsequent photocatalytic reaction and facilitates the photodegradation of the aromatic ring. Besides, the redshift of Pt/TiO<sub>2</sub>-C is greater than Pt/TiO<sub>2</sub> after illumination, which suggests that more electrons accumulate on the benzene ring and weaken the conjugated π bond [56], thereby further promoting the ring-opening reaction of the aromatic ring. The intermediate species of the photolysis reaction will be explored through *in situ* DRIFTS.

In Fig. 8a and 8b, the band at 1508 cm<sup>−1</sup> is assigned to the skeleton v (C = C) vibrations of the aromatic ring [32], and the band at 1473 cm<sup>−1</sup> is ascribed to the asymmetric v (C-H) deformation vibration of -CH<sub>3</sub>. In Pt/TiO<sub>2</sub>-C, the peak intensity at 1540 cm<sup>−1</sup> belonging to benzaldehyde first decreases and then increases within 30 min, which means the consumption and further accumulation of benzaldehyde. This variation can be proved to facilitate the oxidation of benzaldehyde to benzoic acid. By contrast, the continuous enhancement of this peak intensity in Pt/TiO<sub>2</sub> means that the oxidation process of benzaldehyde to benzoic acid is difficult to occur, indicating a relatively slower oxidation rate. This further proves that the fast pre-activation provides a higher reactants concentration for the photodegradation reaction, which is beneficial to the rapid conversion of intermediate species. Similar to that of 1540 cm<sup>−1</sup>, this kind of variation is also observed over the range of

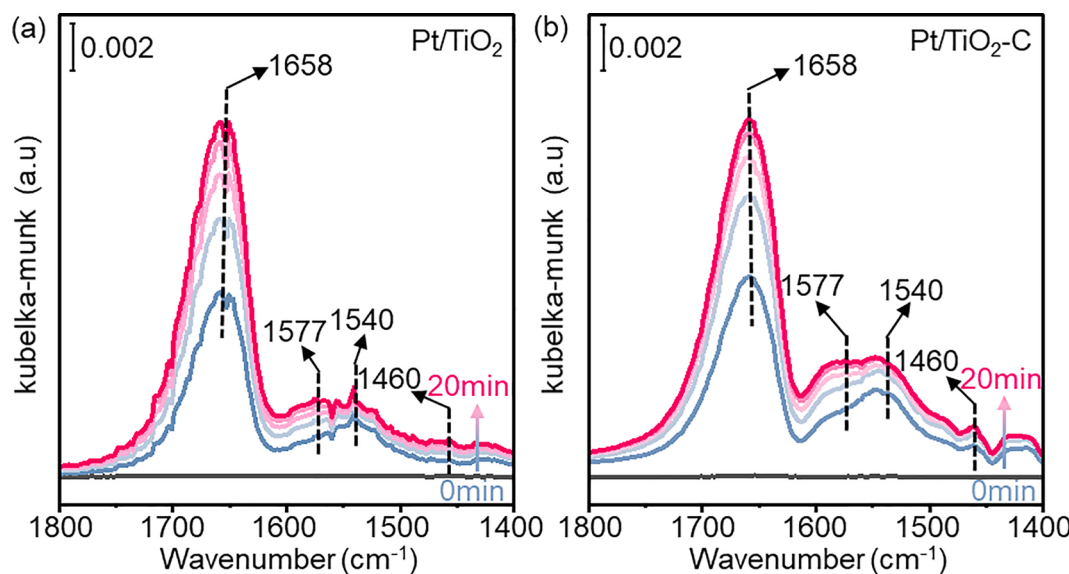


Fig. 6. *In situ* DRIFTS of toluene adsorption over (a) Pt/TiO<sub>2</sub> and (b) Pt/TiO<sub>2</sub>-C.

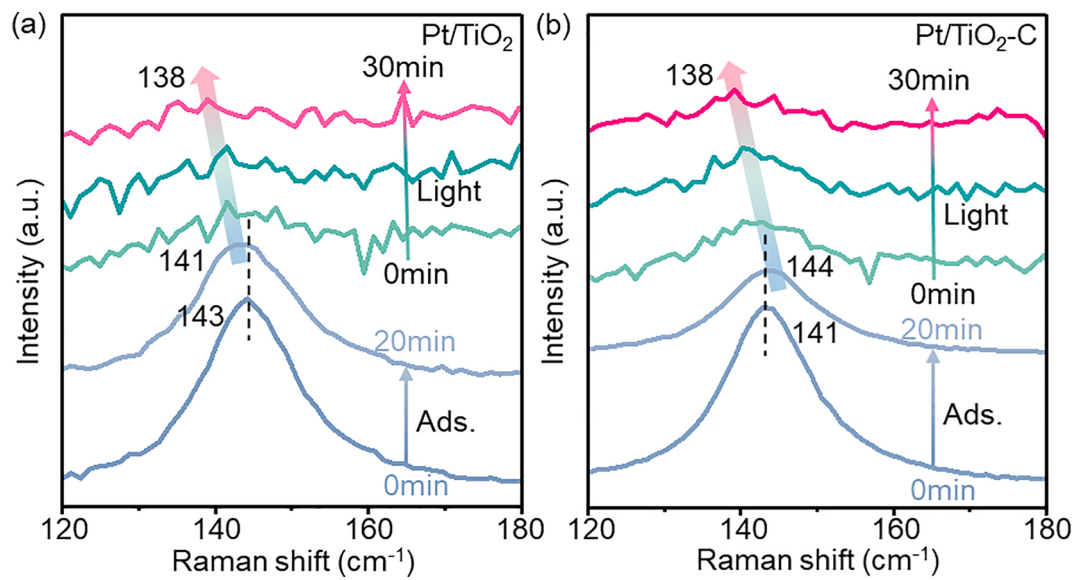


Fig. 7. *In situ* Raman spectra of toluene adsorption and degradation for (a) Pt/TiO<sub>2</sub> and (b) Pt/TiO<sub>2</sub>-C.

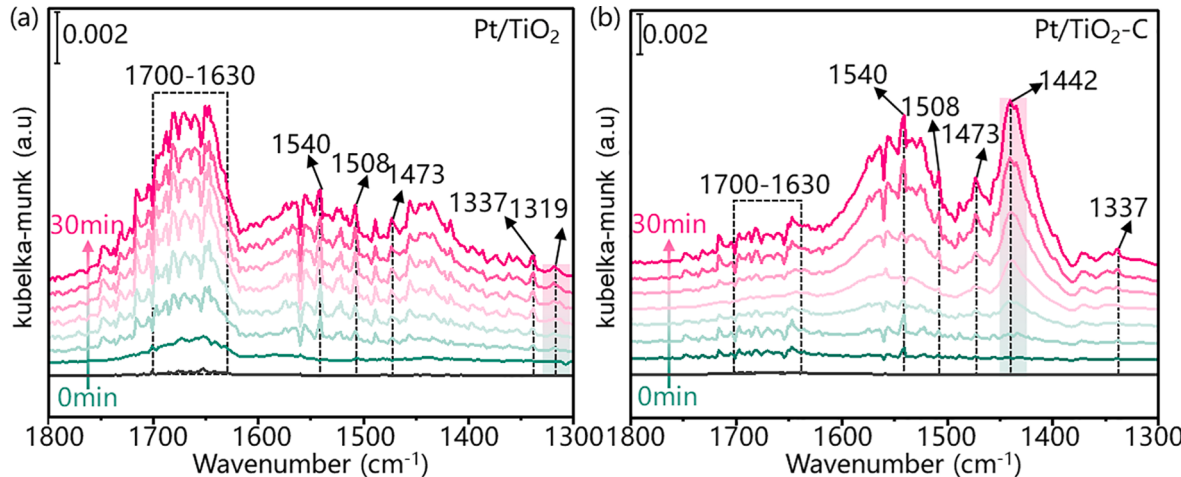


Fig. 8. *In situ* DRIFTS of toluene degradation for (a) Pt/TiO<sub>2</sub> and (b) Pt/TiO<sub>2</sub>-C.

1630–1700 cm<sup>-1</sup> for Pt/TiO<sub>2</sub>-C, which is also attributed to the consumption and further accumulation vibration of benzaldehyde [50,57]. The difference can be explained as the Ti<sup>δ+</sup>-Vo-Pt<sup>δ+</sup> interface site which enhances the oxidation capability of the Pt/TiO<sub>2</sub>-C accelerates the deep oxidation of intermediate species. Beyond that, the bands at 1337 cm<sup>-1</sup> belonging to phenol are found over Pt/TiO<sub>2</sub> and Pt/TiO<sub>2</sub>-C [58], suggesting that the conversion of chemically adsorbed benzene to phenol is promoted under illumination. The occurrence of this reaction path is further confirmed by the above-mentioned *in situ* Raman spectroscopy. Moreover, a new peak observed at 1319 cm<sup>-1</sup> is ascribed to maleic anhydride in Pt/TiO<sub>2</sub> [59], whereas another new intense peak that appears at 1442 cm<sup>-1</sup> is associated with the formation of vibration stretching of C-C bonds in the intermediates by •OH directly attacking the aromatic ring in Pt/TiO<sub>2</sub>-C [60].

To understand the degradation process of toluene more clearly, GC-MS is performed to explore the intermediates of different samples during the illumination process. Similar intermediates such as CO<sub>2</sub>, benzene, toluene, phenol, benzoic acid, etc. are observed in two catalysts (Fig. S18). As shown in Fig. 9a and 9b, except for acetaldehyde and glyoxal, new intermediates such as acetic acid, acetone, and aldehyde species (appearing in 1.4, 1.5, and 1.8 min) are also observed in Pt/TiO<sub>2</sub>-C. The generation of these intermediates fully proves that Pt/TiO<sub>2</sub>-C can

realize the direct opening of the benzene ring.

The possible degradation mechanism of toluene over the catalysts is shown in Fig. 10. According to the above analysis, the fast pre-activation of toluene first occurs on -CH<sub>3</sub> through the following reaction route: toluene → benzaldehyde → benzoic acid → benzene. Moreover, the production of phenol intermediates lays the foundation for the subsequent photolysis reaction. Interestingly, the formation of two completely different intermediate products (1319 cm<sup>-1</sup> in Pt/TiO<sub>2</sub>, 1442 cm<sup>-1</sup> in Pt/TiO<sub>2</sub>-C) is observed during the ring-opening process of phenol. This may be caused by the •OH attacking different sites on the benzene ring. Therefore, phenol can be further attacked by the •OH to form maleic anhydride or carbon chain intermediates in the ring-opening process of toluene over Pt/TiO<sub>2</sub>-C and Pt/TiO<sub>2</sub>, respectively. This implies that the Ti<sup>δ+</sup>-Vo-Pt<sup>δ+</sup> interface can more efficiently catalyze the direct opening of the benzene ring than the traditional Pt/TiO<sub>2</sub> interface. According to the above results, it is proved that the Pt/TiO<sub>2</sub>-C with Ti<sup>δ+</sup>-Vo-Pt<sup>δ+</sup> interface structure has been constructed. The production of the interface structure improves the oxidation capability of the Pt/TiO<sub>2</sub>-C, which provides an ideal structure to enhance the photocatalytic activity and deep oxidation capability of toluene.

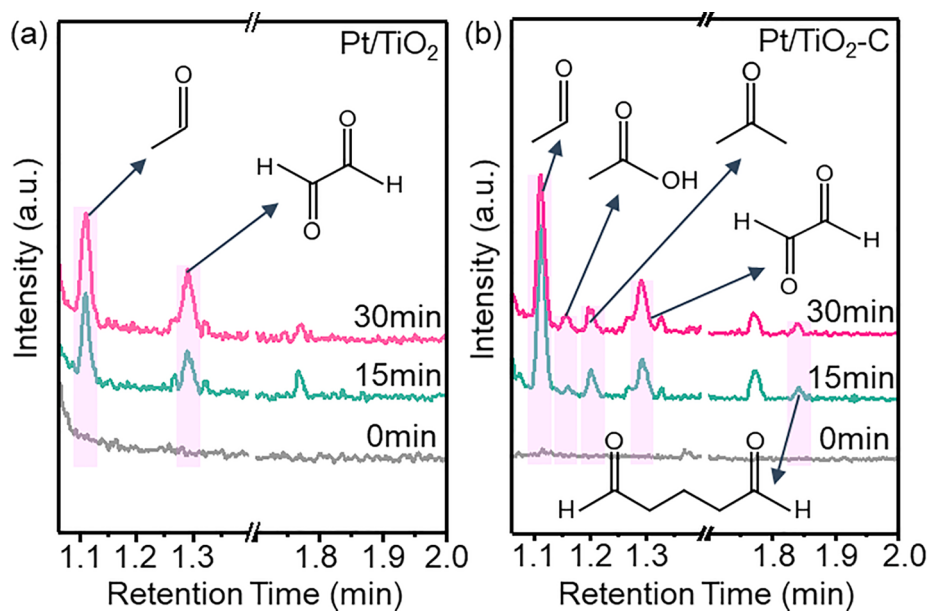


**Fig. 9.** GC-MS profiles of toluene degradation for (a) Pt/TiO<sub>2</sub> and (b) Pt/TiO<sub>2</sub>-C.

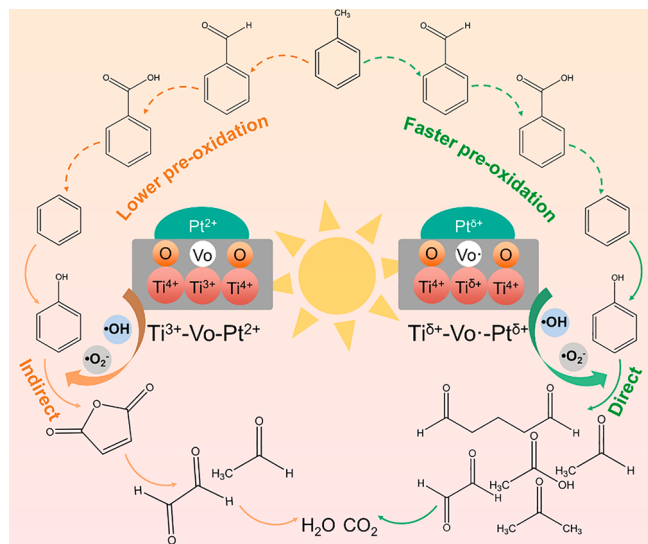


**Fig. 10.** Schematic illustration for photocatalytic degradation of gas toluene over Pt/TiO<sub>2</sub> and Pt/TiO<sub>2</sub>-C.

#### 4. Conclusion

In summary, we successfully regulate the Pt/TiO<sub>2</sub>-C photocatalyst with special Ti<sup>δ+</sup>-Vo<sup>·</sup>-Pt<sup>δ+</sup> interface through the successive reduction–oxidation treatment, which can directly open the benzene ring and further enhance the efficient mineralization of toluene. The Pt/TiO<sub>2</sub>-C exhibits excellent catalytic performance (a degradation rate of 74% and mineralization rate of 85%) for the photocatalytic oxidation of toluene. Combination studies based on XPS, CO-DRIFTS, Raman, and EPR confirm that the construction of the Ti<sup>δ+</sup>-Vo<sup>·</sup>-Pt<sup>δ+</sup> interface structure promotes the oxidation capability of Pt/TiO<sub>2</sub>-C. On the one hand, *in situ* Raman, and *in situ* DRIFTS demonstrate that Ti<sup>δ+</sup>-Vo<sup>·</sup>-Pt<sup>δ+</sup> interface site facilitates the faster pre-activation of chemisorbed toluene, simultaneously triggering more abundant intermediate species for photolysis reaction. On the other hand, GC-MS indicates that the production of more reactive oxygen species promotes the direct ring-opening reaction of the benzene ring. Tailoring of MSI via reduction–oxidation treatment

is thus an effective method to enhance the oxidation capability of Pt/TiO<sub>2</sub> system, which brings broad prospects for purifying air pollution.

#### Declaration of Competing Interest

The authors declare that they have no known competing financial interests or personal relationships that could have appeared to influence the work reported in this paper.

#### Acknowledgements

We acknowledge the support of the National Key R&D Program of China (2017YFE0132400).

#### Appendix A. Supplementary data

Supplementary data to this article can be found online at <https://doi.org/10.1016/j.cej.2021.134209>.

#### References

- [1] S. Gligorovski, J.P.D. Abbatt, An indoor chemical cocktail, *Science*. 359 (6376) (2018) 632–633, <https://doi.org/10.1126/science.aar6837>.
- [2] C. He, J. Cheng, X. Zhang, M. Douthwaite, S. Pattisson, Z. Hao, Recent advances in the catalytic oxidation of volatile organic compounds: A review based on pollutant sorts and sources, *Chem. Rev.* 119 (7) (2019) 4471–4568, <https://doi.org/10.1021/acs.chemrev.8b00408.s001>.
- [3] T. Saltherammer, Y. Zhang, J. Mo, H.M. Koch, C.J. Weschler, Assessing human exposure to organic pollutants in the indoor environment, *Angew. Chem. Int. Ed.* 57 (38) (2018) 12228–12263, <https://doi.org/10.1002/anie.201711023>.
- [4] S. Weon, E. Choi, H. Kim, J.Y. Kim, H.-J. Park, S.-m. Kim, W. Kim, W. Choi, Active {001} facet exposed TiO<sub>2</sub> nanotubes photocatalyst filter for volatile organic compounds removal: from material development to commercial indoor air cleaner application, *Environ. Sci. Technol.* 52 (16) (2018) 9330–9340, <https://doi.org/10.1021/acs.est.8b02282>.
- [5] T.D. Bui, A. Kimura, S. Ikeda, M. Matsumura, Determination of oxygen sources for oxidation of benzene on TiO<sub>2</sub> photocatalysts in aqueous solutions containing molecular oxygen, *J. Am. Chem. Soc.* 132 (24) (2010) 8453–8458, <https://doi.org/10.1021/ja102305e>.
- [6] J. Tripathy, K. Lee, P. Schmuki, Tuning the selectivity of photocatalytic synthetic reactions using modified TiO<sub>2</sub> nanotubes, *Angew. Chem. Int. Ed.* 53 (46) (2014) 12605–12608, <https://doi.org/10.1002/anie.201406324>.
- [7] M. Zeng, Y. Li, M. Mao, J. Bai, L. Ren, X. Zhao, Synergistic effect between photocatalysis on TiO<sub>2</sub> and thermocatalysis on CeO<sub>2</sub> for gas-phase oxidation of benzene on TiO<sub>2</sub>/CeO<sub>2</sub> nanocomposites, *ACS Catal.* 5 (6) (2015) 3278–3286, <https://doi.org/10.1021/acscatal.5b00292>.

- [8] A. Migani, L. Blancafort, Excitonic interfacial proton-coupled electron transfer mechanism in the photocatalytic oxidation of methanol to formaldehyde on  $\text{TiO}_2(110)$ , *J. Am. Chem. Soc.* 138 (49) (2016) 16165–16173, <https://doi.org/10.1021/jacs.6b1106710.1021/jacs.6b11067.s001>.
- [9] X. Zhu, C. Jin, X.-S. Li, J.-L. Liu, Z.-G. Sun, C. Shi, X. Li, A.-M. Zhu, Photocatalytic formaldehyde oxidation over plasmonic  $\text{Au}/\text{TiO}_2$  under visible light: moisture indispensability and light enhancement, *ACS Catal.* 7 (10) (2017) 6514–6524, <https://doi.org/10.1021/acscatal.7b0165810.1021/acscatal.7b01658.s001>.
- [10] J. Liu, P. Wang, W. Qu, H. Li, L. Shi, D. Zhang, Nanodiamond-decorated  $\text{ZnO}$  catalysts with enhanced photocorrosion-resistance for photocatalytic degradation of gaseous toluene, *Appl. Catal. B: Environ.* 257 (2019), 117880, <https://doi.org/10.1016/j.apcatb.2019.117880>.
- [11] Z. Shayegan, C.-S. Lee, F. Haghighat,  $\text{TiO}_2$  photocatalyst for removal of volatile organic compounds in gas phase – A review, *Chem. Eng. J.* 334 (2018) 2408–2439, <https://doi.org/10.1016/j.cej.2017.09.153>.
- [12] K. Vikrant, S. Weon, K.-H. Kim, M. Sillanpää, Platinized titanium dioxide ( $\text{Pt}/\text{TiO}_2$ ) as a multi-functional catalyst for thermocatalysis, photocatalysis, and photothermal catalysis for removing air pollutants, *Applied Materials Today*. 23 (2021), 100993, <https://doi.org/10.1016/j.apmt.2021.100993>.
- [13] M. Xu, S. Yao, D. Rao, Y. Niu, N. Liu, M.I. Peng, P. Zhai, Y.I. Man, L. Zheng, B. Wang, B. Zhang, D. Ma, M. Wei, Insights into interparticle synergistic catalysis over  $\text{Ni}@\text{TiO}_{2-x}$  catalyst toward water-gas shift reaction, *J. Am. Chem. Soc.* 140 (36) (2018) 11241–11251, <https://doi.org/10.1021/jacs.8b0311710.1021/jacs.8b03117.s001>.
- [14] H. Wang, L. Wang, D. Lin, X. Feng, Y. Niu, B. Zhang, F.S. Xiao, Strong metal-support interactions on gold nanoparticle catalysts achieved through Le Chatelier's principle, *Nat. Catal.* 4 (5) (2021) 418–424, <https://doi.org/10.1038/s41929-021-00611-3>.
- [15] A. Parastaei, V. Muravei, E. Huertas Osta, A.J.F. van Hoof, T.F. Kimpel, N. Kosinov, E.J.M. Hensen, Boosting  $\text{CO}_2$  hydrogenation via size-dependent metal-support interactions in cobalt/ceria-based catalysts, *Nat. Catal.* 3 (6) (2020) 526–533, <https://doi.org/10.1038/s41929-020-0459-4>.
- [16] W. Zhu, Z. Wu, G.S. Foo, X. Gao, M. Zhou, B. Liu, G.M. Veith, P. Wu, K.L. Browning, H.N. Lee, H. Li, S. Dai, H. Zhu, Taming interfacial electronic properties of platinum nanoparticles on vacancy-abundant boron nitride nanosheets for enhanced catalysis, *Nat. Commun.* 8 (1) (2017) 15291, <https://doi.org/10.1038/ncomms15291>.
- [17] Y.U. Guo, S. Mei, K. Yuan, D.-J. Wang, H.-C. Liu, C.-H. Yan, Y.-W. Zhang, Low-temperature  $\text{CO}_2$  methanation over  $\text{CeO}_2$ -supported Ru single atoms nanoclusters, and nanoparticles competitively tuned by strong metal-support interactions and h-spillover effect, *ACS Catal.* 8 (7) (2018) 6203–6215, <https://doi.org/10.1021/acscatal.7b0446910.1021/acscatal.7b04469.s001>.
- [18] C. Hernandez Mejia, T.W. van Deelen, K.P. de Jong, Activity enhancement of cobalt catalysts by tuning metal-support interactions, *Nat. Commun.* 9 (1) (2018) 4459, <https://doi.org/10.1038/s41467-018-06903-w>.
- [19] Z. Liu, B. Jia, Y. Zhang, M. Haneda, Engineering the metal-support interaction on  $\text{Pt}/\text{TiO}_2$  catalyst to boost the  $\text{H}_2$ -SCR of  $\text{NO}_x$ , *Ind. Eng. Chem. Res.* 59 (31) (2020) 13916–13922, <https://doi.org/10.1021/acs.iecr.0c01792>.
- [20] T.W. van Deelen, C. Hernández Mejía, K.P. de Jong, Control of metal-support interactions in heterogeneous catalysts to enhance activity and selectivity, *Nat. Catal.* 2 (11) (2019) 955–970, <https://doi.org/10.1038/s41929-019-0364-x>.
- [21] T. Matsui, T. Okanishi, K. Fujiwara, K. Tsutsui, R. Kikuchi, T. Takeguchi, K. Eguchi, Effect of reduction-oxidation treatment on the catalytic activity over tin oxide supported platinum catalysts, *Sci. Technol. Adv. Mater.* 7 (6) (2016) 524–530, <https://doi.org/10.1016/j.stam.2006.02.020>.
- [22] A.M. Gänzler, M. Casapu, F. Maurer, H. Störmer, D. Gerthsen, G. Ferré, P. Vernoux, B. Bornmann, R. Frahm, V. Mürzin, M. Nachtegaal, M. Votsmeier, J.-D. Grunwaldt, Tuning the  $\text{Pt}/\text{CeO}_2$  interface by in situ variation of the Pt particle size, *ACS Catal.* 8 (6) (2018) 4800–4811, <https://doi.org/10.1021/acscatal.8b0033010.1021/acscatal.8b00330.s001>.
- [23] W. Qu, P. Wang, M. Gao, J.-y. Hasegawa, Z. Shen, Q. Wang, R. Li, D. Zhang, Delocalization effect promoted the indoor air purification via directly unlocking the ring-opening pathway of toluene, *Environ. Sci. Technol.* 54 (15) (2020) 9693–9701, <https://doi.org/10.1021/acs.est.0c0290610.1021/acs.est.0c02906.s001>.
- [24] Y. Wang, C. Jiang, Y. Le, B. Cheng, J. Yu, Hierarchical honeycomb-like  $\text{Pt}/\text{NiFe-LDH}/\text{RGO}$  nanocomposite with excellent formaldehyde decomposition activity, *Chem. Eng. J.* 365 (2019) 378–388, <https://doi.org/10.1016/j.cej.2019.01.187>.
- [25] Y. Qin, H. Li, J. Lu, F. Meng, C. Ma, Y. Yan, M. Meng, Nitrogen-doped hydrogenated  $\text{TiO}_2$  modified with  $\text{CdS}$  nanorods with enhanced optical absorption, charge separation and photocatalytic hydrogen evolution, *Chem. Eng. J.* 384 (2020), 123275, <https://doi.org/10.1016/j.cej.2019.123275>.
- [26] J. Zhang, H. Wang, L. Wang, S. Ali, C. Wang, L. Wang, X. Meng, B.o. Li, D.S. Su, F.-S. Xiao, Wet-chemistry strong metal-support interactions in titania-supported Au catalysts, *J. Am. Chem. Soc.* 141 (7) (2019) 2975–2983, <https://doi.org/10.1021/jacs.8b1086410.1021/jacs.8b10864.s001>.
- [27] S. Liu, W. Xu, Y. Niu, B. Zhang, L. Zheng, W. Liu, L. Li, J. Wang, Ultrastable Au nanoparticles on titania through an encapsulation strategy under oxidative atmosphere, *Nat. Commun.* 10 (1) (2019) 5790, <https://doi.org/10.1038/s41467-019-13755-5>.
- [28] S. Liu, H. Qi, J. Zhou, W. Xu, Y. Niu, B. Zhang, Y. Zhao, W. Liu, Z. Ao, Z. Kuang, L. Li, M. Wang, J. Wang, Encapsulation of platinum by titania under an oxidative atmosphere: contrary to classical strong metal-support interactions, *ACS Catal.* 11 (10) (2021) 6081–6090, <https://doi.org/10.1021/acscatal.1c0134710.1021/acscatal.1c01347.s001>.
- [29] J. Li, M. Zhang, Z. Guan, Q. Li, C. He, J. Yang, Synergistic effect of surface and bulk single-electron-trapped oxygen vacancy of  $\text{TiO}_2$  in the photocatalytic reduction of  $\text{CO}_2$ , *Appl. Catal. B: Environ.* 206 (2017) 300–307, <https://doi.org/10.1016/j.apcatb.2017.01.025>.
- [30] H. Zhang, Y. Li, J. Wang, N. Wu, H. Sheng, C. Chen, J. Zhao, An unprecedent hydride transfer pathway for selective photocatalytic reduction of  $\text{CO}_2$  to formic acid on  $\text{TiO}_2$ , *Appl. Catal. B: Environ.* 284 (2021), 119692, <https://doi.org/10.1016/j.apcatb.2020.119692>.
- [31] J. Ni, W. Wang, D. Liu, Q. Zhu, J. Jia, J. Tian, Z. Li, X. Wang, Z. Xing, Oxygen vacancy-mediated sandwich-structural  $\text{TiO}_{2-x}$ /ultrathin  $\text{g-C}_3\text{N}_4/\text{TiO}_{2-x}$  direct Z-scheme heterojunction visible-light-driven photocatalyst for efficient removal of high toxic tetracycline antibiotics, *J. Hazard. Mater.* 408 (2021), 124432, <https://doi.org/10.1016/j.jhazmat.2020.124432>.
- [32] F. Wang, J. Deng, S. Impeng, Y. Shen, T. Yan, G. Chen, L. Shi, D. Zhang, Unraveling the effects of the coordination number of Mn over  $\alpha\text{-MnO}_2$  catalysts for toluene oxidation, *Chem. Eng. J.* 396 (2020), 125192, <https://doi.org/10.1016/j.cej.2020.125192>.
- [33] L.Y. Lin, S. Kavadiya, X. He, W.N. Wang, B.B. Karakocak, Y.C. Lin, M.Y. Berezin, P. Biswas, Engineering stable Pt nanoparticles and oxygen vacancies on defective  $\text{TiO}_2$  via introducing strong electronic metal-support interaction for efficient  $\text{CO}_2$  photoreduction, *Chem. Eng. J.* 389 (2020), 123450, <https://doi.org/10.1016/j.cej.2019.123450>.
- [34] J. Luo, H. Tang, X. Tian, S. Hou, X. Li, L.I. Du, S. Liao, Highly selective  $\text{TiN}$ -supported highly dispersed Pt catalyst: ultra active toward hydrogen oxidation and inactive toward oxygen reduction, *ACS Appl. Mater. Interfaces*. 10 (4) (2018) 3530–3537, <https://doi.org/10.1021/acsami.7b1515910.1021/acsami.7b15159.s001>.
- [35] H. Wang, J.X. Liu, L.F. Allard, S. Lee, J. Liu, H. Li, J. Wang, J. Wang, S.H. Oh, W. Li, M. Flytzani Stephanopoulos, M. Shen, B.R. Goldsmith, M. Yang, Surpassing the single-atom catalytic activity limit through paired Pt-O-Pt ensemble built from isolated Pt1 atoms, *Nat. Commun.* 10 (1) (2019) 3808, <https://doi.org/10.1038/s41467-019-11856-9>.
- [36] X. Du, Y. Huang, X. Pan, B. Han, Y. Su, Q. Jiang, M. Li, H. Tang, G. Li, B. Qiao, Size-dependent strong metal-support interaction in  $\text{TiO}_2$  supported Au nanocatalysts, *Nat. Commun.* 11 (1) (2020) 5811, <https://doi.org/10.1038/s41467-020-19484-4>.
- [37] L. Li, L. Li, L. Wang, X. Zhao, Z. Hua, Y. Chen, X. Li, X. Gu, Enhanced catalytic decomposition of formaldehyde in low temperature and dry environment over silicate-decorated titania supported sodium-stabilized platinum catalyst, *Appl. Catal. B: Environ.* 277 (2020), 119216, <https://doi.org/10.1016/j.apcatb.2020.119216>.
- [38] L. Chen, J. Ye, Y. Yang, P. Yin, H. Feng, C. Chen, X. Zhang, M. Wei, D.G. Truhlar, Catalytic conversion furfuryl alcohol to tetrahydrofurfuryl alcohol and 2-methylfuran at terrace, step, and corner sites on Ni, *ACS Catal.* 10 (13) (2020) 7240–7249, <https://doi.org/10.1021/acscatal.0c144110.1021/acscatal.0c144110.s001>.
- [39] F. Jiang, L. Zeng, S. Li, G. Liu, S. Wang, J. Gong, Propane dehydrogenation over  $\text{Pt}/\text{TiO}_2\text{-Al}_2\text{O}_3$  Catalysts, *ACS Catal.* 5 (1) (2014) 438–447, <https://doi.org/10.1021/c501279v>.
- [40] M.M. Khan, S.A. Ansari, D. Pradhan, M.O. Ansari, D.H. Han, J. Lee, M.H. Cho, Band gap engineered  $\text{TiO}_2$  nanoparticles for visible light induced photoelectrochemical and photocatalytic studies, *J. Mater. Chem. A*. 2 (3) (2014) 637–644, <https://doi.org/10.1039/c3ta14052k>.
- [41] M. Trejo Valdez, S.R. Hernández Guzmán, M.E. Manríquez Ramírez, H. Sobral, H. Martínez Gutiérrez, C. Torres Torres, Removal of aqueous chromium and environmental  $\text{CO}_2$  by using photocatalytic  $\text{TiO}_2$  doped with tungsten, *J. Hazard. Mater.* 370 (2019) 196–202, <https://doi.org/10.1016/j.jhazmat.2018.05.008>.
- [42] S. Sun, J.i. Wu, M. Watanabe, T. Akbay, T. Ishihara, Single-electron-trapped oxygen vacancy on ultrathin  $\text{WO}_3\cdot0.33\text{H}_2\text{O}$  (100) facets suppressing backward reaction for promoted  $\text{H}_2$  evolution in pure water splitting, *J. Phys. Chem. Lett.* 10 (11) (2019) 2998–3005, <https://doi.org/10.1021/acs.jpclett.9b01032>.
- [43] J. Huo, Y. Hu, H. Jiang, C. Li, In situ surface hydrogenation synthesis of  $\text{Ti}^{3+}$  self-doped  $\text{TiO}_2$  with enhanced visible light photoactivity, *Nanoscale*. 6 (15) (2014) 9078–9084, <https://doi.org/10.1039/c4nr00972j>.
- [44] L. Xu, S. Wang, T. Zhang, F. Chen, Photo-induced re-modulation of Pt particles loaded on V-TiO<sub>2</sub> for enhanced CO photocatalytic oxidation, *Catal. Sci. Technol.* 7 (17) (2017) 3698–3701, <https://doi.org/10.1039/c7cy01220a>.
- [45] H. Li, F. Ren, J. Liu, Q. Wang, Q. Li, J. Yang, Y. Wang, Endowing single-electron-trapped oxygen vacancy self-modified titanium dioxide with visible-light photocatalytic activity by grafting Fe(III) nanocluster, *Appl. Catal. B: Environ.* 172–173 (2015) 37–45, <https://doi.org/10.1016/j.apcatb.2015.02.008>.
- [46] H. Li, H. Shang, Y. Li, X. Cao, Z. Yang, Z. Ai, L. Zhang, Interfacial charging-decharging strategy for efficient and selective aerobic NO oxidation on oxygen vacancy, *Environ. Sci. Technol.* 53 (12) (2019) 6964–6971, <https://doi.org/10.1021/acs.est.9b0128710.1021/acs.est.9b01287.s001>.
- [47] G. Yin, X. Huang, T. Chen, W. Zhao, Q. Bi, J. Xu, Y. Han, F. Huang, Hydrogenated blue titania for efficient solar to chemical conversions: Preparation, characterization, and reaction mechanism of  $\text{CO}_2$  reduction, *ACS Catal.* 8 (2) (2018) 1009–1017, <https://doi.org/10.1021/acscatal.7b0347310.1021/acscatal.7b03473.s001>.
- [48] Y. Nosaka, A.Y. Nosaka, Generation and detection of reactive oxygen species in photocatalysis, *Chem. Rev.* 117 (17) (2017) 11302–11336, <https://doi.org/10.1021/acs.chemrev.7b00161>.
- [49] C.M. Huang, G.T. Pan, P.Y. Peng, T.C.K. Yang, In situ DRIFT study of photocatalytic degradation of gaseous isopropanol over  $\text{BiVO}_4$  under indoor illumination, *J. Mol. Catal. A: Chem.* 327 (1–2) (2010) 38–44, <https://doi.org/10.1016/j.molcata.2010.05.009>.

- [50] X. Yang, X. Ma, X. Yu, M. Ge, Exploration of strong metal-support interaction in zirconia supported catalysts for toluene oxidation, *Appl. Catal. B: Environ.* 263 (2020), 118355, <https://doi.org/10.1016/j.apcatb.2019.118355>.
- [51] X. Li, J. Li, Y. Shi, M. Zhang, S. Fan, Z. Yin, M. Qin, T. Lian, X. Li, Rational design of cobalt and nitrogen Co-doped carbon hollow frameworks for efficient photocatalytic degradation of gaseous toluene, *J. Colloid Interface Sci.* 528 (2018) 45–52, <https://doi.org/10.1016/j.jcis.2018.05.067>.
- [52] W. Yang, Z. Su, Z. Xu, W. Yang, Y. Peng, J. Li, Comparative study of  $\alpha$ -,  $\beta$ -,  $\gamma$ - and  $\delta$ - $\text{MnO}_2$  on toluene oxidation: Oxygen vacancies and reaction intermediates, *Appl. Catal. B: Environ.* 260 (2020) 118150, <https://doi.org/10.1016/j.apcatb.2019.118150>.
- [53] Y. Zhou, C. Chen, N. Wang, Y. Li, H. Ding, Stable  $\text{Ti}^{3+}$  self-doped anatase-rutile mixed  $\text{TiO}_2$  with enhanced visible light utilization and durability, *J. Phys. Chem. C* 120 (11) (2016) 6116–6124, <https://doi.org/10.1021/acs.jpcc.6b0065510.1021/acs.jpcc.6b00655.s001>.
- [54] F. Zhang, X. Zhu, J. Ding, Z. Qi, M. Wang, S. Sun, J. Bao, C. Gao, Mechanism study of photocatalytic degradation of gaseous toluene on  $\text{TiO}_2$  with weak-bond adsorption analysis using in situ far infrared spectroscopy, *Catal. Lett.* 144 (6) (2014) 995–1000, <https://doi.org/10.1007/s10562-014-1213-9>.
- [55] D.R. Sahu, L.Y. Hong, S.C. Wang, J.L. Huang, Synthesis, analysis and characterization of ordered mesoporous  $\text{TiO}_2/\text{SBA}-15$  matrix: Effect of calcination temperature, *Microporous Mesoporous Mater.* 117 (3) (2009) 640–649, <https://doi.org/10.1016/j.micromeso.2008.08.013>.
- [56] L. Wang, S.V. Khare, V. Chirita, D.D. Johnson, A.A. Rockett, A.I. Frenkel, N. H. Mack, R.G. Nuzzo, Origin of bulklike structure and bond length disorder of  $\text{Pt}_{37}$  and  $\text{Pt}_6\text{Ru}_{31}$  clusters on carbon: Comparison of theory and experiment, *J. Am. Chem. Soc.* 128 (1) (2006) 131–142, <https://doi.org/10.1021/ja053896m>.
- [57] L. Zhao, Z. Zhang, Y. Li, X. Leng, T. Zhang, F. Yuan, X. Niu, Y. Zhu, Synthesis of  $\text{Ce}\text{aMnO}_x$  hollow microsphere with hierarchical structure and its excellent catalytic performance for toluene combustion, *Appl. Catal. B: Environ.* 245 (2019) 502–512, <https://doi.org/10.1016/j.apcatb.2019.01.005>.
- [58] R. Chen, J. Li, J. Sheng, W. Cui, X. Dong, P. Chen, H. Wang, Y. Sun, F. Dong, Unveiling the unconventional roles of methyl number on the ring-opening barrier in photocatalytic decomposition of benzene, toluene and o-xylene, *Appl. Catal. B: Environ.* 278 (2020) 119318, <https://doi.org/10.1016/j.apcatb.2020.119318>.
- [59] Y. Lyu, C. Li, X. Du, Y. Zhu, Y. Zhang, S. Li, Catalytic oxidation of toluene over  $\text{MnO}_2$  catalysts with different Mn (II) precursors and the study of reaction pathway, *Fuel* 262 (2020), 116610, <https://doi.org/10.1016/j.fuel.2019.116610>.
- [60] Z. Jiang, C. Chen, M. Ma, Z. Guo, Y. Yu, C. He, Rare-earth element doping-promoted toluene low-temperature combustion over mesostructured  $\text{CuM CeO}_x$  ( $\text{M} = \text{Y}, \text{Eu}, \text{Ho}, \text{and Sm}$ ) catalysts: the indispensable role of in situ generated oxygen vacancies, *Catal. Sci. Technol.* 8 (22) (2018) 5933–5942, <https://doi.org/10.1039/c8cy01849a>.